RSC Advances

PAPER

View Article Online
View Journal | View Issue

Cite this: *RSC Adv.*, 2022, **12**, 2425

Fe/Co/N–C/graphene derived from Fe/ZIF-67/graphene oxide three dimensional frameworks as a remarkably efficient and stable catalyst for the oxygen reduction reaction†

Junchao Xiong,[ab] Xiaohong Chen,*[a] Yupan Zhang,[a] Yue Lu,[c] Xundao Liu,[c] Yafei Zheng,[a] Yongming Zhang[a] and Jun Lin[b]

Received 3rd December 2021
Accepted 10th January 2022

DOI: 10.1039/d1ra08817c

rsc.li/rsc-advances

The development of non-noble metal catalysts with high-performance, long stability and low-cost is of great importance for fuel cells, to promote the oxygen reduction reaction (ORR). Herein, Fe/Co/N–C/graphene composites were easily prepared by using Fe/ZIF-67 loaded on graphene oxide (GO). The Fe/Co/porous carbon nanoparticles were uniformly dispersed on graphene with high specific surface area and large porosity, which endow high nitrogen doping and many more active sites with better ORR performance than the commercial 20 wt% Pt/C. Therefore, Fe/Co/N–C/graphene composites exhibited excellent ORR activity in alkaline media, with higher initial potential (0.91 V) and four electron process. They also showed remarkable long-term catalytic stability with 96.5% current retention after 12 000 s, and outstanding methanol resistance, compared with that of 20 wt% Pt/C catalysts. This work provides an effective strategy for the preparation of non-noble metal-based catalysts, which could have significant potential applications, such as in lithium–air batteries and water-splitting devices.

1. Introduction

Fuel cells are extremely important energy conversion devices, which can efficiently convert hydrogen and other clean energy into electrical energy.[1–5] However, the energy conversion efficiency of fuel cells is limited by the slow kinetics of the oxygen reduction reaction (ORR) in the cathode. Although researchers have been actively working on the development of non-precious metal electrocatalysts for the ORR, catalysts with high activity and durability are urgently needed.[6–18] So far, transition metal (M) and nitrogen co-doped carbon materials containing M–N_x active centers are considered as the most promising catalyst materials. The transition metal–nitrogen–carbon (M–N–C) catalysts could provide more active sites to improve the ORR performance.[19–27] Three-dimensional cobalt–nitrogen double-doped porous carbon (3D Co–N/C) was prepared and exhibited remarkable ORR properties, which were attributed to Co doping and high content of pyridine nitrogen.[28] Co doped N–C (Co/N–C) catalysts were synthesized by direct pyrolysis of glucose doped with cobalt metals, which also showed excellent ORR performance.[29] Novel three-dimensional mesoporous Co/N–C (Co@Co/N–C–A NHs) catalysts with a nanosheet network structure were further developed.[30] Due to the presence of a small quantity of Co nanoparticles, the half-wave potential and limiting current density of the Co doped catalysts are superior to those of the commercial 20 wt% Pt/C.[31]

Although some non-noble metal supported nitrogen–carbon catalysts have higher initial potentials and half-wave potentials than that of commercial Pt/C catalysts, their durability still remains a great challenge. Recently, many efforts have been made to improve the durability of the electrochemical catalysts, such as increasing the surface area and enhancing the degree of graphitization.[32–34] Heteroatom doped carbon materials derived from metal–organic frameworks (MOFs) have been considered as the ideal ORR catalyst materials, because of their adjustable and porous structure.[35–42] Zeolitic imidazolate frameworks (ZIFs), one of the most promising precursor materials among the MOF family, possessed large surface area, high porosity and adjustable pore size.[43–45] More importantly, ZIFs are rich in nitrogen and can offer active center metals to afford high activity for fuel cells.[46–49] However, the calcination from ZIFs will destroy their ordered structure and porous morphology, leading to the poor ORR performance, which is attributed to the low graphitization, poor conductivity and electron migration ability of ZIFs materials. With NaCl as additives, porous Co/N co-doped catalysts were prepared by the calcination of ZIF-67, which showed excellent ORR performance.[50] Co, Fe, Ni co-doped nitrogen-rich hollow carbon

[a]*Institute of Advanced Materials, North China Electric Power University, Beijing, 102206, China. E-mail: xhchen200905@ncepu.edu.cn*
[b]*School of New Energy, North China Electric Power University, Beijing, 102206, China*
[c]*School of Materials Science and Engineering, University of Jinan, Jinan, 250022, China*

† Electronic supplementary information (ESI) available. See DOI: 10.1039/d1ra08817c

(CoFeNi/NC) derived from PVP/ZIF-8/ZIF-67 exhibited relatively good ORR catalytic activity. The addition of Fe and Ni can enhance the graphitization degree and the specific surface area of the CoFeNi/NC, to substantially enhance the ORR activity.[51] To further enhance the ORR performance of ZIFs-based catalysts, it is urgent to prepare catalysts with high specific surface area and high electrical conductivity.

Generally, graphene oxide (GO) with large surface area, rich graphitic carbon and excellent electrical conductivity is widely used in fuel cell and other fields.[52–56] Herein, we developed a simple and effective preparation method of Fe/Co/N–C/graphene composites, derived from Fe/ZIF-67 (2-methylimidazole cobalt/iron) loaded on GO. Interestingly, Fe/Co/N–C/graphene composites showed excellent ORR catalytic activity in the alkaline electrolyte. The initial potential and half-wave potential, limiting current density and electron transfer number (n) of Fe/Co/N–C/graphene composites were better than that of 20 wt% Pt/C catalysts. Moreover, Fe/Co/N–C/graphene composites also displayed excellent stability and methanol resistance in the alkaline media.

2. Materials and experimental

2.1 Materials

Graphite oxide powder was purchased from Nanjing XFNANO Materials Tech Co., Ltd. Methanol (99.9%), potassium hydroxide (90%), ferric nitrate nonahydrate (98%) and 2-methylimidazole and cobalt(II) nitrate hexahydrate were bought from Shanghai Titan Technology Co., Ltd. Nafion solution (5 wt%) was obtained from E. I. Du Pont Company.

2.2 Apparatus

Transmission electron microscopy (TEM, JEOT JEM 2010HT) and scanning electron microscopy (SEM, Tescan Mira 3 XH) (both from Electron Optics Laboratory Co., Ltd., Japan); powder X-ray diffraction (XRD, Bruker, Japan, Smart Lab); Raman spectra (Thermo Fei, Thermo DXR 2xi, USA); X-ray photoelectron spectroscopy (XPS, Thermo Fei, Thermo Scientific Escalab 250xi, USA). Brunauer–Emmett–Teller (BET, Quantachrome Ins USA Quadrasorb EVO); Electrochemical measurements (CHI 660D, Chenhua, China).

2.3 Synthesis of Co/N–C, Co/N–C/graphene, Fe/Co/N–C and Fe/Co/N–C/graphene composites

Firstly, 100 mL GO/methanol dispersion (2 mg mL^{-1}) was prepared, as the A solution. 0.60 g cobalt nitrate hexahydrate and 0.10 g ferric nitrate nonahydrate were dissolved in 22 mL methanol and then stirred for several minutes, as the B solution. 20 mL A solution was added to the B solution, to keep stirring for at least 1 h to obtain C solution. And then 1.37 g 2-methylimidazole was dissolved in 42 mL methanol and stirred for 10 min, which was quickly added to the C solution. After stirring for 24 h, the products were collected by centrifugation at 9000 rpm for 5 min, washed with methanol for 3 times, and then dried at 80 °C in oven for 24 h, to obtain Fe/ZIF-67/GO. The ZIF-67, ZIF-67/GO and Fe/ZIF-67 were synthesized according to the above procedures. Then ZIF-67, ZIF-67/GO, Fe/ZIF-67 and Fe/ZIF-67/GO was finally pyrolyzed in 800 °C argon environment for 2 h at a heating rate of 5 °C min^{-1}, to finally obtain Co/N–C, Co/N–C/graphene, Fe/Co/N–C and Fe/Co/N–C/graphene composites separately.

3. Results and discussion

The overall preparation process of Fe/Co/N–C/graphene is shown in Scheme 1. First, Co^{2+} and Fe^{3+} ions were adsorbed to the oxygen-containing functional groups on GO, as the nucleation sites for the growth of ZIF crystals. After the addition of 2-

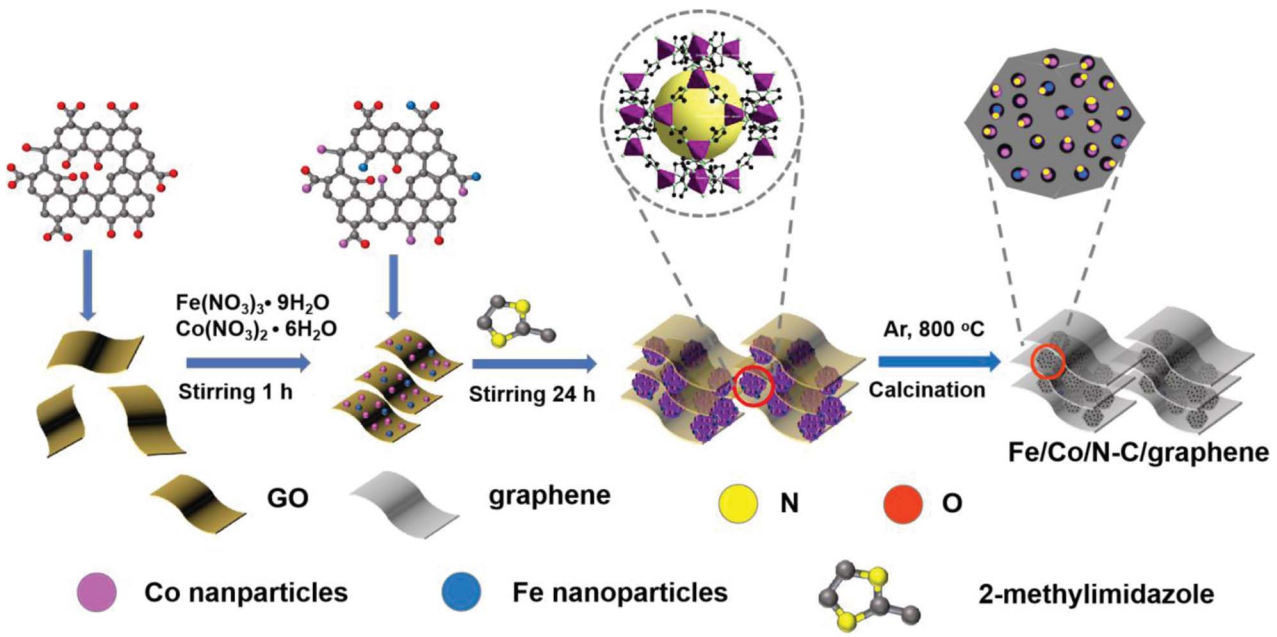

Scheme 1 Schematic for the synthesis of Fe/Co/N–C/graphene composites.

methylimidazole, the ZIF-67 nucleus grew on the surface of GO, forming the ZIF-67 structure loaded on GO (Fe/ZIF-67/GO). After pyrolysis at 800 °C, Fe/Co/N–C/graphene with high specific surface area was obtained.

To observe the morphology of the prepared samples, scanning electron microscopy (SEM) of ZIF-67, ZIF-67/GO, Fe/ZIF-67, Co/N–C, Co/N–C/graphene and Fe/Co/N–C was characterized. Fig. 1a shows ZIF-67 has regular polyhedral shape and uniform size (about 1 μm), confirming the successful synthesis of ZIF-67 crystals. Fig. 1b shows the carbon skeleton of Co/N–C derived from ZIF-67 was collapsed and contracted, losing its original regular shape and structure. The surface of Co/N–C becomes rough and the size decreases, mainly due to the decomposition of imidazole and the cleavage of organic ligands during pyrolysis. After the addition of GO, ZIF-67 nanoparticles become larger and are unevenly dispersed on the surface (Fig. 1c). There are many microspheres in Co/N–C/graphene (Fig. 1d). Even though the introduction of GO can promote the formation of graphitic nitrogen, the mass transfer efficiency in the microspheres may not be high due to the lack of pores. Therefore, Fe/ZIF-67 presents regular polyhedral shape (Fig. 1e), due to the Fe addition. Moreover, the morphology of Fe/ZIF-67 with smooth surface and large size (Fig. 1f) could be retained during the pyrolysis process.

Fig. 2a–c show SEM images of Fe/ZIF-67/GO under different magnification factors. Fe/ZIF-67/GO remains regular polyhedral structure with the addition of GO and Fe. Fe/ZIF-67 nanoparticles is uniformly dispersed on the GO surface, which can prevent the collapse of the carbon skeleton and the accumulation of GO during the pyrolysis process. Fe/Co/N–C nanoparticles with a size of about 30 nm are distributed on the graphene (Fig. 2d–f). To get more information of the surface area and porosity of the Fe/Co/N–C/graphene, the N_2 adsorption and desorption isotherms of ZIF-67, Fe/ZIF-67/GO, Co/N–C and Fe/Co/N–C/graphene are shown in Fig. 2g and h. ZIF-67 and Fe/ZIF-67/GO exhibit large specific surface areas (293.5 and 573.1 $m^2 g^{-1}$), and abundant macropores and mesopores (2.5 and 4.9 nm) (Fig. 2h). The surface area and average pore diameter of Co/N–C/graphene is 78.4 $m^2 g^{-1}$ and 6.7 nm (Fig. S1†), while the specific surface areas and large pore size of Co/N–C and Fe/Co/N–C/graphene are (131.1 $m^2 g^{-1}$, 7.3 nm) and (150.4 $m^2 g^{-1}$ and 8.1 nm), respectively. The larger pores and smaller surface area of Fe/Co/N–C/graphene may be caused by the co-addition of Fe^{3+} and GO. The increase in the pore size of Fe/Co/N–C/graphene can ensure fass diffusion of oxygen, leading to the improvement of the catalytic activity of Fe/Co/N–C/graphene.

To get more information of Co/N–C and Fe/Co/N–C/graphene structure, the transmission electron microscopy (TEM) characterization of Co/N–C and Fe/Co/N–C/graphene was

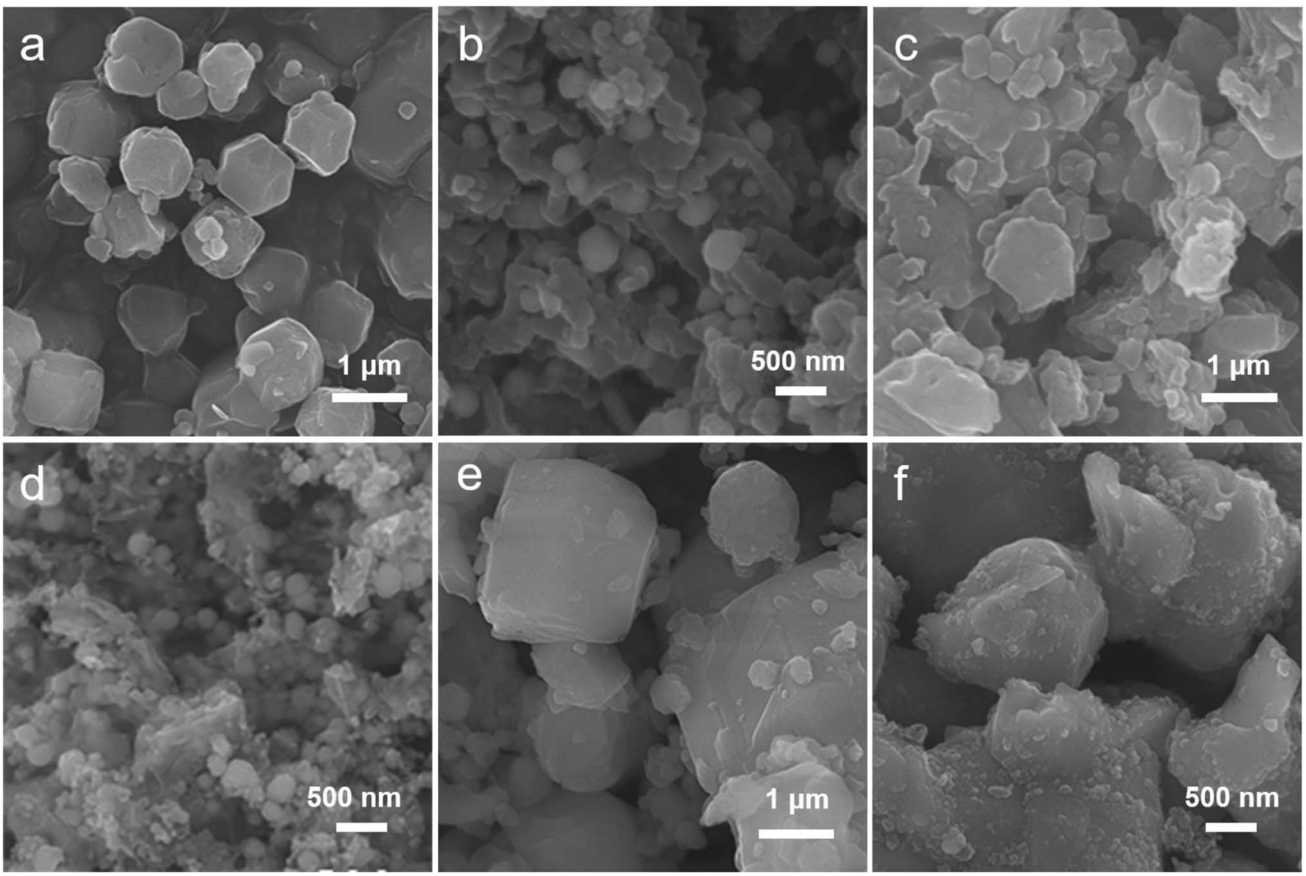

Fig. 1 SEM images of (a) ZIF-67, (b) Co/N–C, (c) ZIF-67/GO, (d) Co/N–C/graphene, (e) Fe/ZIF-67 and (f) Fe/Co/N–C composites.

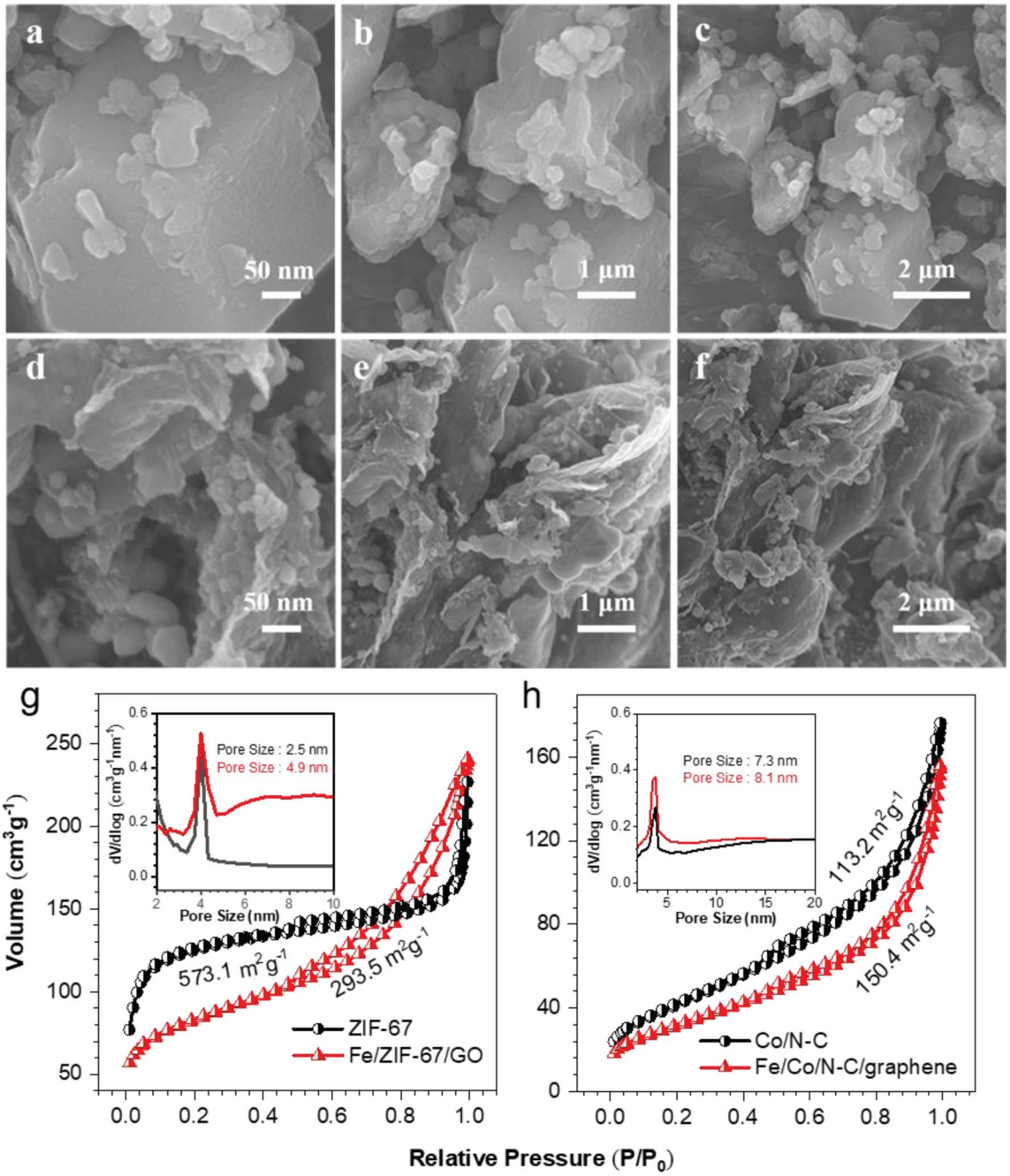

Fig. 2 SEM images at different magnification of (a–c) Fe/ZIF-67/GO and (d–f) Fe/Co/N–C/graphene; (g and h) N_2 adsorption/desorption isotherms (inset: pore size distribution) of ZIF-67, Fe/ZIF-67/GO, Co/N–C and Fe/Co/N–C/graphene composites.

conducted. The Fe/Co/N–C nanoparticles of Fe/Co/N–C/graphene were uniformly dispersed on the graphene, with the well-distributed particle size (about 10–30 nm) (Fig. 3a). In comparison, the Co/N–C nanoparticles were agglomerated (Fig. S2†), without the addition of Fe and graphene. High resolution TEM (HRTEM) of Fe/Co/N–C/graphene composites shows that the lattice spacing is 0.191 nm and 0.202 nm, respectively, which corresponds to the crystal plane of metal Co (101) and Fe–Co (330). These results indicate the Co and Fe–Co alloy nanoparticles appear together in Fe/Co/N–C/graphene, which could offer more active sites for enhancing ORR performance. It is also clear from Fig. 3b that Fe/Co/N–C particles are uniformly dispersed on the surface of graphene, indicating that graphitic carbon in Fe/Co/N–C/graphene around metal ions was easily formed, which also enhances the catalytic activity of ORR. Furthermore, Fig. 3e shows a high-angle annular dark field scanning transmission electron microscope (HAADF-STEM) and corresponding element mapping image of Fe/Co/N–C/graphene, which shows the carbon and nitrogen dopants are uniformly distributed in the Fe/Co/N–C nanoparticles.

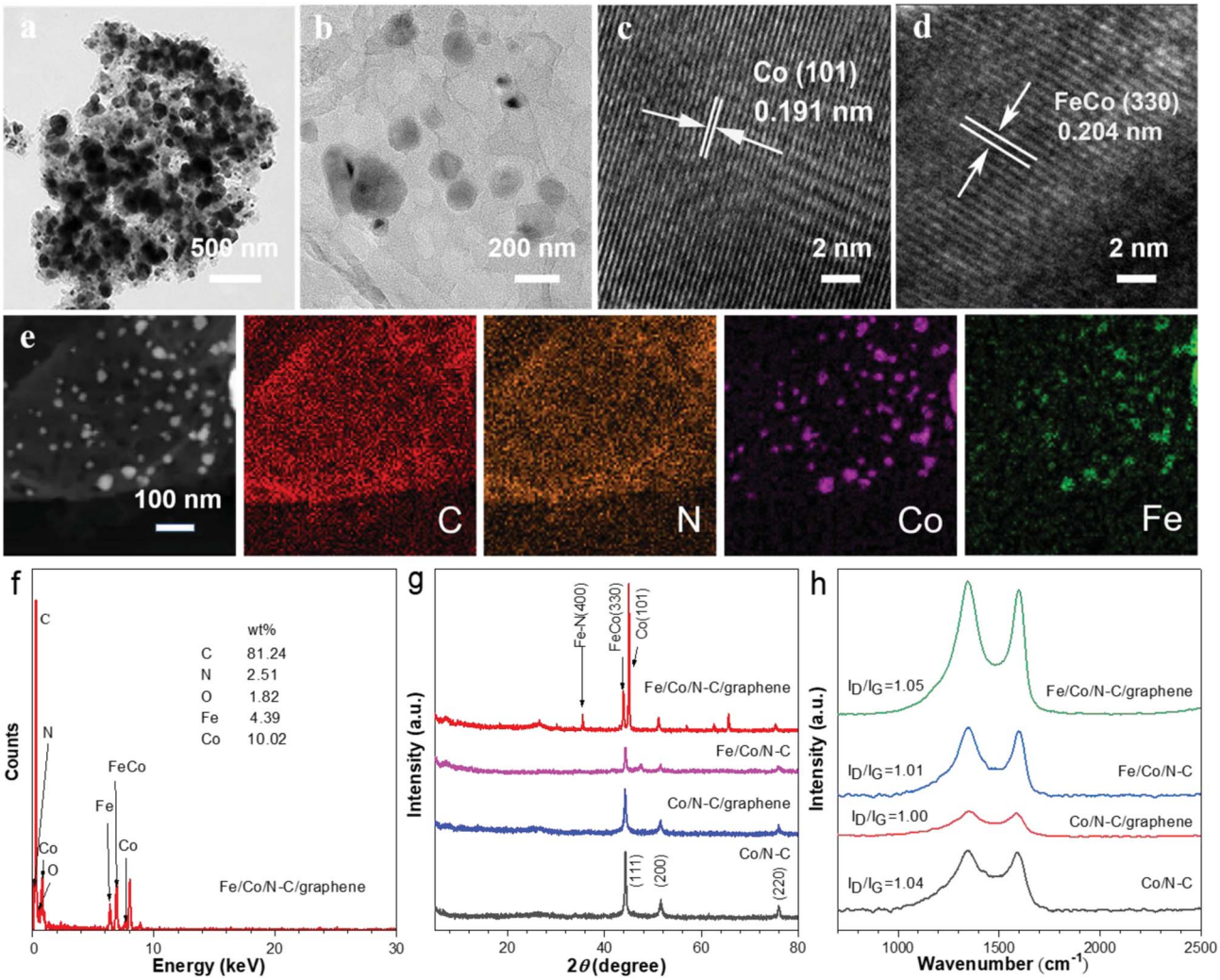

Fig. 3 (a) TEM, (b–d) HRTEM, (e) corresponding elemental mapping images and (f) EDS spectrum of Fe/Co/N–C/graphene; (g and h) XRD patterns and Raman spectra of Co/N–C, Co/N–C/graphene, Fe/Co/N–C and Fe/Co/N–C/graphene composites.

Meanwhile, Co and Fe elements are well distributed and match with N region, indicating that Co–N_x and Fe–N_x active sites may be formed in these samples. The energy dispersion spectrometer (EDS) results of Fe/Co/N–C/graphene composites showed the weight content of C, N, Co and Fe (Fig. 3f) is 81.24 wt%, 2.51 wt%, 1.82 wt% and 4.39 wt%, respectively, which is consistent with the HAADF-STEM results.

The XRD spectra of Co/N–C, Co/N–C/graphene, Fe/Co/N–C and Fe/Co/N–C/graphene were further analyzed. The peaks of ZIF-67, ZIF-67/GO, Fe/ZIF-67 and Fe/ZIF-67/GO are similar (Fig. S3†), indicating that the addition of Fe^{3+} and GO has little influence on the crystal structure of ZIF-67. As shown in Fig. 3g, three diffraction peaks of Co/N–C, Co/N–C/graphene and Fe/Co/N–C composites were at 44.31°, 51.68° and 76.08°, respectively, which are consistent with the Co (111), Co (200) and Co (220) (PDF#150806) crystal plane, indicating the successful formation of Co crystals in these composites. The diffraction peaks at 35.45°, 43.84° and 45.00° were also observed in Fe/Co/N–C/graphene, which are well matched with Fe–N (400), Fe–Co (330) and Co (101) (PDF#510740) crystal plane, and also consistent with the TEM results. Furthermore, Raman spectra of Co/N–C, Co/N–C/graphene, Fe/Co/N–C and Fe/Co/N–C/graphene were performed to analyze their defect degree (Fig. 3h), in which two characteristic carbon peaks were shown, corresponding to D band peak of 1348 cm^{-1} and G band peak of 1599 cm^{-1}, respectively. The intensity ratio of the two peaks (I_D/I_G) was used to evaluate the defect degree of the catalysts.[57] The I_D/I_G of Fe/Co/N–C/graphene composites is 1.05, which is higher than that of Co/N–C (1.04), Co/N–C/graphene (1.00) and Fe/Co/N–C (1.01) composites, due to many more defect sites in the carbon skeleton produced by Fe dopants and graphene. This may provide more active ORR sites and have good mass transfer ability.

To probe the chemical element composition and chemical state, XPS tests of Co/N–C and Fe/Co/N–C/graphene were further performed. The C, N, O, Co and Fe elements of the Fe/Co/N–C/graphene composites are shown in Fig. 4a and Table 1. Graphitic-N and pyridinic-N play important roles in ORR

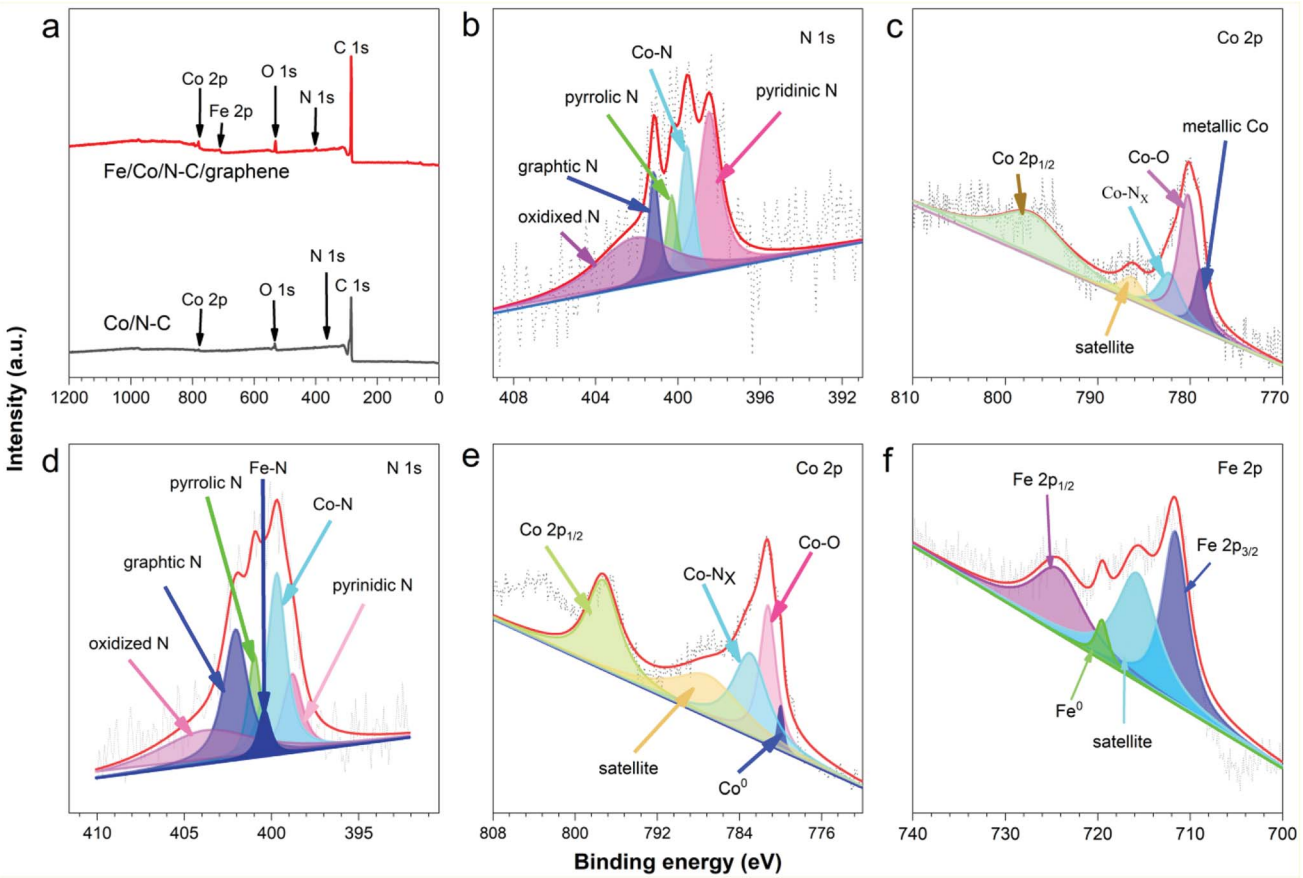

Fig. 4 (a) XPS survey scan of Co/N–C and Fe/Co/N–C/graphene; the XPS spectra of (b) N 1s, (c) Co 2p for Co/N–C and (d) N 1s, (e) Co 2p, (f) Fe 2p for Fe/Co/N–C/graphene.

Table 1 The different elemental content of Co/N–C and Fe/Co/N–C/graphene composites by XPS

Samples	C 1s (%)	N 1s (%)	O 1s (%)	Co 2p (%)	Fe 2p (%)
Co/N–C	93.04	1.36	4.87	0.73	—
Fe/Co/N–C/graphene	89.42	2.02	6.41	1.3	0.85

performance,[58] which is of great significance to the understanding of electrocatalysis. The high resolution N 1s (Fig. 4d) of Fe/Co/N–C/graphene can be divided into six types: pyridine-N (398.8 eV), graphitic-N (401.5 eV), pyrrolic-N (400.8 eV), Co–N (399.5 eV), Fe–N (399.6 eV) and oxygen-N (403.8 eV), and the corresponding atomic contents are 11.36, 27.32, 8.58, 25.44, 5.84 and 21.46% (Table 2), respectively. Compared with that of Co/N–C, the overall N content of Fe/Co/N–C/graphene increased, especially with the sharp increase of the graphitic-N and Co–N contents. These results suggested that the Fe/Co/N–C/graphene owns high content of graphitic-N, higher specific surface area, more Co–N_x and Fe–N_x active sites, and better mass transfer efficiency, which is attributed to the addition of Fe and GO.

The Co–N_x and Fe–N_x are one of the most effective active sites to improve the catalytic activity of ORR performance under alkaline conditions. As seen in Fig. 4e, two main peaks of the Co 2p spectra of Fe/Co/N–C/graphene were observed, corresponding to $Co2p_{1/2}$ (797.2 eV) and $Co2p_{3/2}$ (780.5 eV), respectively. $Co2p_{3/2}$ can be divided into Co^0 (780.0 eV), Co–O (781.2 eV), Co–N_x (782.9 eV) and satellite peak (787.0 eV), respectively. Co–O may be due to the oxidation of Co on the surface of GO, and Co–

Table 2 The different nitrogen atomic content of Co/N–C and Fe/Co/N–C/graphene composites by XPS

Samples	Oxidized-N (%)	Graphitic-N (%)	Pyrrolic-N (%)	Pyridinic-N (%)	Co–N (%)	Fe–N (%)
Co/N–C	34.78	10.75	8.07	32.96	13.44	—
Fe/Co/N–C/graphene	21.46	27.32	8.58	11.36	25.44	5.84

N confirms the existence of Co–N_x, which can increase the catalytic activity of ORR under alkaline conditions.[59] The Fe 2p spectra (Fig. 4f) show Fe $2p_{3/2}$ (711.6 eV), Fe $2p_{1/2}$ (724.3 eV), satellite peak (716.1 eV) and Fe^0 (719.5 eV), indicating that Fe not only acts as an additive to form uniform dispersion and many more pores of ZIF-67, but can form the active sites of Fe–N_x to enhance the ORR performance. In addition, Co^0 in Co 2p and Fe^0 in Fe 2p confirm the presence of Fe–Co alloy, which can also improve the catalytic activity of Fe/Co/N–C/graphene.

To evaluate the ORR performance of Co/N–C, Co/N–C/graphene, Fe/Co/N–C and Fe/Co/N–C/graphene, their CV measurements were carried out at a potential scan rate of 100 mV s^{-1} through a three-electrode system in O_2-saturated 0.1 M KOH.[60] As seen in Fig. 5a, the CV curves of Co/N–C, Co/N–C/graphene, Fe/Co/N–C and Fe/Co/N–C/graphene show large cathodic reduction peaks at 0.81 V, 0.84 V, 0.78 V and 0.87 V, respectively, indicating the Fe/Co/N–C/graphene composite has a larger oxygen reduction peak. The LSV curves of Co/N–C, Co/N–C/graphene, Fe/Co/N–C and Fe/Co/N–C/graphene composites were recorded in Fig. 4b. Fe/Co/N–C/graphene composites have excellent ORR electrocatalytic activity with the limiting current density of 6.78 mA cm^{-2}, which is slightly higher than that of 20 wt% Pt/C (6.63 mA cm^{-2}). It can be seen from Table 3 that Co/N–C/graphene has a corrected initial potential (E_{onset}) at 0.89 V and half-wave potential ($E_{1/2}$) at 0.83 V, which is higher than that of Co/N–C (0.86 V, 0.81 V) and Fe/Co/N–C (0.85 V, 0.81 V). This is attributed to the enhanced electrical conductivity and increased activity sites with the addition GO. However, the change of E_{onset} and $E_{1/2}$ is relatively small with the addition of Fe. Furthermore, with the co-addition of GO and Fe, the E_{onset} and $E_{1/2}$ of Fe/Co/N–C/graphene are 0.91 V and 0.85 V, which were higher than that of 20 wt% Pt/C (0.91 V, 0.82 V), indicating that Fe/Co/N–C/graphene composites had a remarkable ORR activity. This is due to the enhanced electrical conductivity and

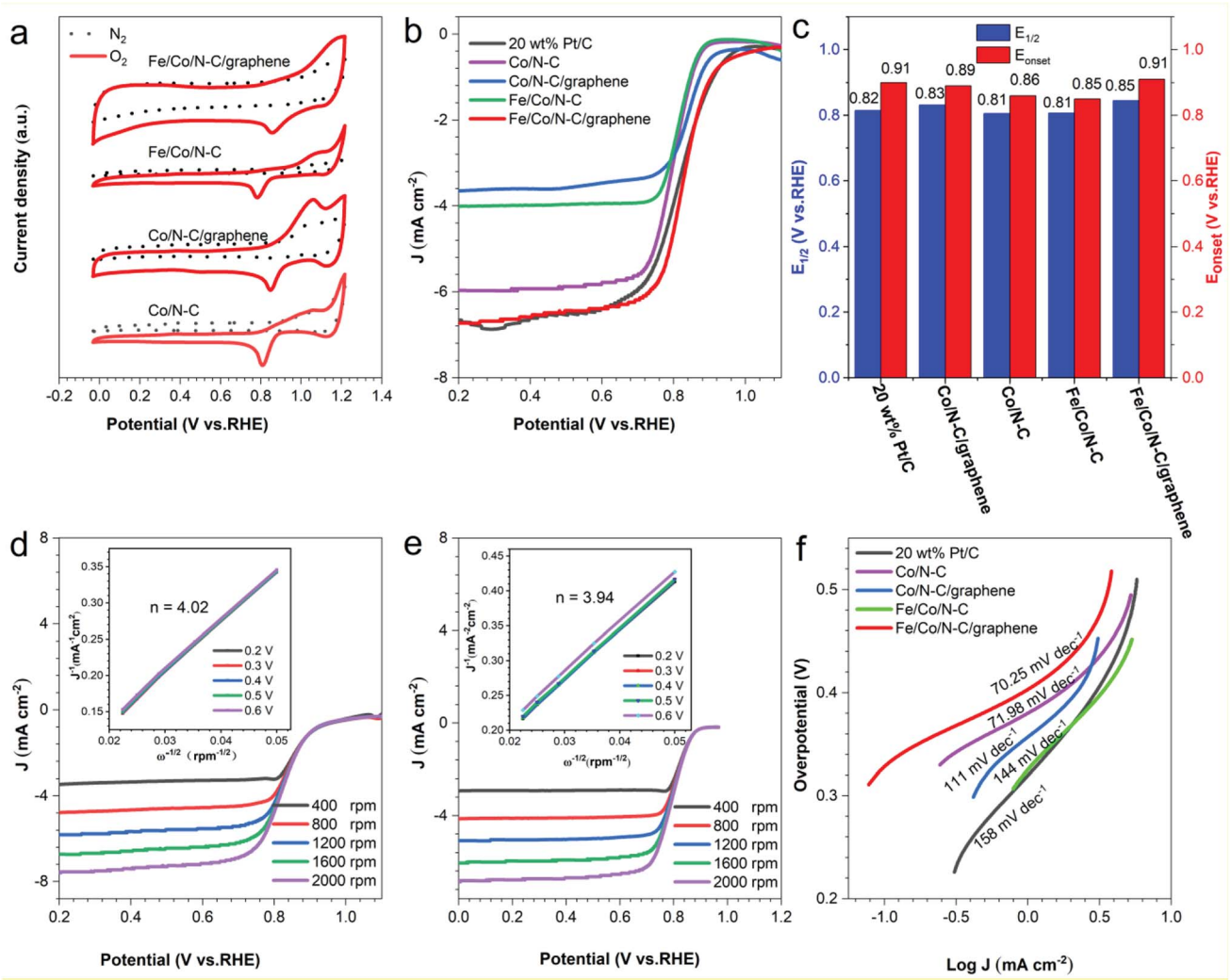

Fig. 5 (a) CV curves of Co/N–C, Co/N–C/graphene, Fe/Co/N–C and Fe/Co/N–C/graphene in O_2- and N_2-saturated 0.1 M KOH electrolyte; (b) LSV curves on a RDE in O_2-saturated 0.1 M KOH at a 1600 rpm, (c) on set potential (E_{onset}) (red) and half-wave potential ($E_{1/2}$) (blue) and (f) Tafel plots of Co/N–C; Co/N–C/graphene; Fe/Co/N–C; Fe/Co/N–C/graphene and 20 wt% Pt/C; (d and e) LSV curves of Fe/Co/N–C/graphene and Co/N–C at different rotating speeds rotating speeds in O_2-saturated 0.1 M KOH solution (inset: corresponding *K–L* plots of within different potentials, respectively).

Table 3 ORR activity comparison for Co/N–C, Co/N–C/graphene, Fe/Co/N–C and Fe/Co/N–C/graphene composites

Samples	Co/N–C	Co/N–C/graphene	Fe/Co/N–C	Fe/Co/N–C/graphene	20 wt% Pt/C
E_{onset} [a] (V *vs.* RHE)	0.86	0.89	0.85	0.91	0.91
$E_{1/2}$ [b] (V *vs.* RHE)	0.81	0.83	0.81	0.85	0.82
n [c]	3.94	3.13	3.80	4.02	4.00

[a] E_{onset} = on set potential. [b] $E_{1/2}$ = half-wave potential. [c] n = electron transport number.

Table 4 Comparison of the ORR catalytic performances of Fe/Co/N–C/graphene with those of other ZIF-derived heteroatom-doped carbon catalysts reported in literature

Samples	E_{onset} (V *vs.* RHE)	$E_{1/2}$ (V *vs.* RHE)	J_L (mA cm^{-2})	n	Ref.
Fe/Co/N–C/graphene	0.91	0.85	6.78	4.02	This work
ZIF-67-900	0.91	0.82	5.33	3.52	23
NGR	0.87	0.74	5.63	3.40	30
CoNC-CNFs	0.92	0.80	5.91	3.98	37
Zn–Co–ZIF/GO-920	0.91	0.81	6.23	3.97	45
CoNC–1NaCl-800	0.94	0.84	5.43	4.17	49
CNT-900	0.93	0.81	4.98	3.99	61
FeCo/Co2P@NPCF	0.85	0.79	4.89	3.85	62

more Co–N_x and Fe–N_x active sites with the coincorporation of Fe and GO. The limiting current density of the Co/N–C, Co/N–C/graphene, Fe/Co/N–C and Fe/Co/N–C/graphene (Fig. 5d–f, S4a and c†) increased with the increasing rotation rate from 400 to 2000 rpm, suggesting higher diffusion rate of O_2 to improve ORR activity.

According to the Koutecky–Levich (*K–L*) diagram (Fig. 5d, e inset, S4b and d†), the average electron transfer number (n) of Fe/Co/N–C and Co/N–C/graphene composites at 0.2–0.6 V was calculated to be 3.13 and 3.80, respectively. Moreover, the n of Co/N–C and Fe/Co/N–C/graphene composites in the range of 0.2–0.6 V was 3.94 and 4.02, respectively, indicating that it was a favorable 4e$^-$ oxygen reduction pathway in the ORR process, which produces water instead of intermediate products such as H_2O_2 during the ORR process. Furthermore, the electrochemical activity comparison between Fe/Co/N–C/graphene and other previously reported catalysts is summarized in the Table 4, which shows Fe/Co/N–C/graphene has the better ORR performance. From the slope of the corresponding Tafel curve (Fig. 5f), the Tafel slope of Fe/Co/N–C/graphene is 70.25 mV dec^{-1}, which was lower than that of Co/N–C (71.98 mV dec^{-1}), Co/N–C/graphene (111 mV dec^{-1}), Fe/Co/N–C (144 mV dec^{-1}) and 20 wt% Pt/C (158 mV dec^{-1}). These results further confirmed the excellent ORR activity of Fe/Co/N–C/graphene composites, due to the synergistic effect among the graphene, graphitic-N, Co–N_x and Fe–N_x activity sites.

In addition, to further assess the mechanism of enhanced ORR activity on Fe/Co/N–C/graphene, we identified the electron transfer numbers and the peroxide (H_2O_2) yield using a rotating ring disk electrode (RRDE). As shown in Fig. 6a, the H_2O_2 yield is below 8% and the n value within the potential of 0.2–0.9 V is 3.84 during the ORR process, which is better than Co/N–C (Fig. S5†). This demonstrates a dominant four-electron ORR catalytic pathway. Therefore, the RRDE result for Fe/Co/N–C/graphene is in accordance with that of the RDE.

To gain further insight into the catalytic efficiencies of the Co/N–C, Co/N–C/graphene, Fe/Co/N–C and Fe/Co/N–C/graphene, the turnover frequencies (TOF) and C_{dl} of Co/N–C and Fe/Co/N–C/graphene were calculated. Compared to that of Co/N–C (19.25 mol O_2 min^{-1} catalyst min^{-1}), the TOF of Fe/Co/N–C/graphene catalyst displayed a higher value of 49.18 mol O_2 min^{-1} catalyst min^{-1}, indicating the increasing average

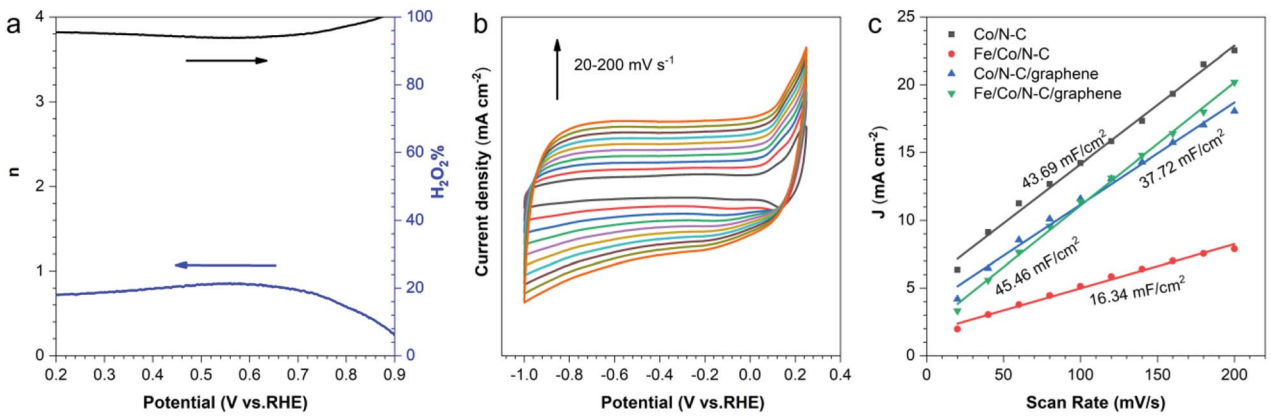

Fig. 6 (a) Electronic transfer number and H_2O_2 yield scurves of Fe/Co/N–C/graphene on a RRDE at 1600 rpm during ORR, (b) non-faradic CVs of Fe/Co/N–C/graphene electrode at various scan rates, (c) current density difference *vs.* potential scan rate plots.

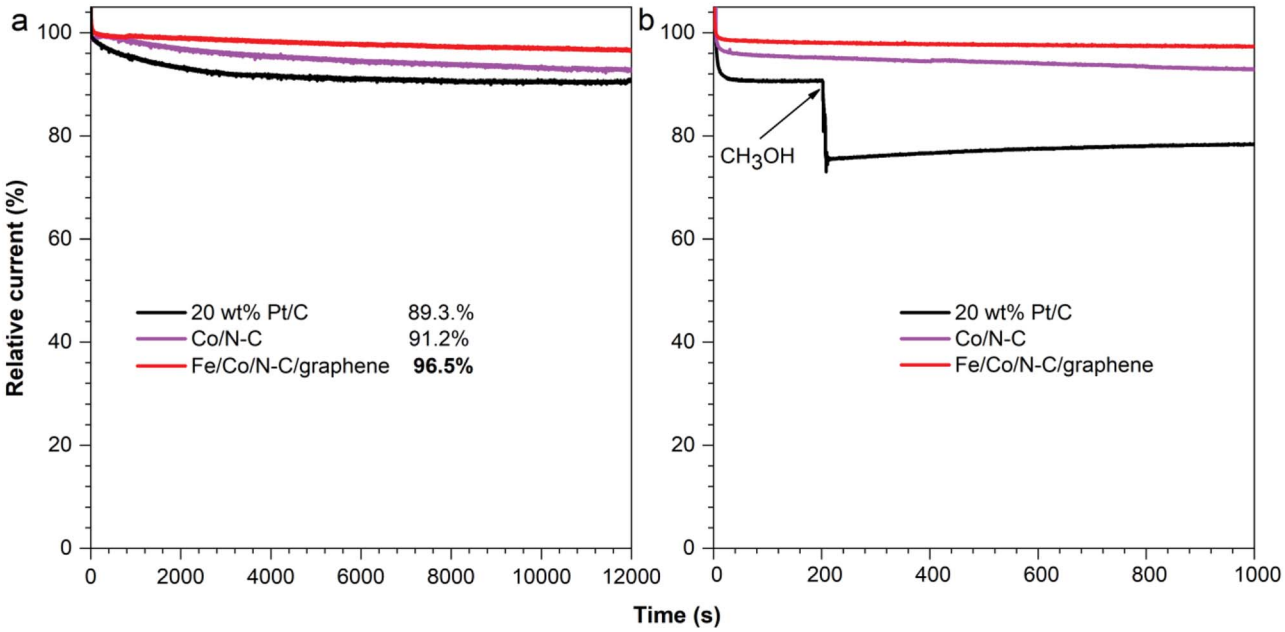

Fig. 7 (a) *i*–*t* chronoamperometric response for 12 000 s in O_2-saturated 0.1 M KOH and (b) methanol tolerance under a potential of 0.62 V with 3 wt% methanol addition at around 200 s of Co/N–C, Fe/Co/N–C/graphene and 20 wt% Pt/C. The rotation speed is at 1600 rpm.

intrinsic active sites in Fe/Co/N–C/graphene. C_{dl} was used to evaluate the largest electrochemical active surface area (ECSA) of the electrode, which can be measured *via* the CVs in non-faradic potential range at various scan rates. The half value of linear slope for ΔJ *vs.* scan rate plots represents the C_{dl}. Fig. 6b and Fig. S6† show the CV curves of Co/N–C, Co/N–C/graphene, Fe/Co/N–C and Fe/Co/N–C/graphene at different scanning rates, whose C_{dl}s were obtained according to the corresponding calculation. As seen in the Fig. 6c, the calculated C_{dl} of Fe/Co/N–C/graphene electrode (45.46 mF cm^{-2}) is higher than that of Fe/Co/N–C (16.34 mF cm^{-2}), Co/N–C (43.69 mF cm^{-2}) and Co/N–C/graphene (37.72 mF cm^{-2}), which indicates the Fe/Co/N–C/graphene has the largest ECSA. Because the catalytic activity of the electrode material is dependent on the ECSA, Fe/Co/N–C/graphene shows the highest catalytic activity.

Apart from the electrocatalytic activity, the long-term stability of the catalysts is the key index for their application in fuel cells. Therefore, the catalytic durability of Co/N–C, Fe/Co/N–C/graphene and 20 wt% Pt/C composites was evaluated by measuring *i*–*t* chronoamperometric response at 0.62 V in O_2-saturated 0.1 M KOH at 1600 rpm. As shown in Fig. 7a, after 12 000 s, 96.5% of the initial current for Fe/Co/N–C/graphene was retained, compared with 91.2% for Co/N–C and 89.3% for 20 wt% Pt/C. The excellent stability of Fe/Co/N–C/graphene is

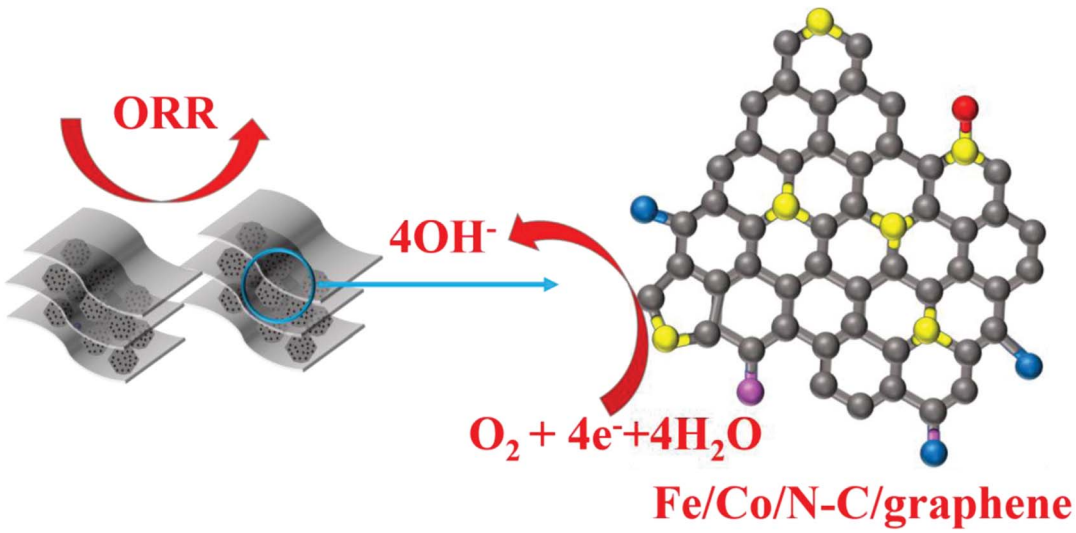

Fig. 8 The schematic diagram of ORR performance of Fe/Co/N–C/graphene composites.

attributed to the increased graphitic carbon of nanoporous carbon particles after the addition of GO. Moreover, methanol solution (3.0 wt%) was added to O_2-saturated 0.1 M KOH solution at 200 s to test the methanol resistance of Co/N–C, Fe/Co/N–C/graphene and 20 wt% Pt/C (Fig. 7b). The current of 20 wt% Pt/C sharply decreased, resulting from the toxic effect of methanol on Pt, while the current of Co/N–C, and Fe/Co/N–C/graphene wasn't changed, demonstrating much better methanol tolerance than 20 wt% Pt/C. These results indicate that Fe/Co/N–C/graphene has better ORR performance, superior durability and excellent methanol resistance, which makes it a promising fuel cell catalyst material as the alternative for the commercial Pt/C catalyst.

As shown from the sketch of the catalytic mechanism in Fig. 8, Fe/Co/N–C/graphene composites exhibited better ORR electrocatalytic activity with the addition of Fe and graphene, which is attributed to the following factors: (1) with the addition of Fe, the porosity of ZIF-67 could be retained during the pyrolysis process. More Co–N_x active sites are provided and Fe–N_x active sites are generated for improving ORR performance; (2) with the addition of graphene, there are high specific surface area and much more active sites to enhance the catalytic activity. The high electrical conductivity of graphene could increase the mass transfer efficiency. These special features endow Fe/Co/N–C/graphene with excellent stability and high electrocatalytic activity.

4. Conclusions

In summary, Fe/Co/N–C/graphene was facilely and successfully prepared by the calcination process combined with GO, Fe and ZIF-67, which have high graphitic nitrogen content, large porosity and Co–N_x, Fe–N_x active sites, thus enhancing the catalytic activity of ORR in alkali media. Furthermore, the Fe/Co/N–C/graphene exhibits the unexpected, remarkably high electrocatalytic ORR activity ($E_{onset} = 0.91$ V, $E_{1/2} = 0.85$ V, $J_L = 6.78$ mA cm^{-2} and $n = 4.02$) in alkali solutions, which also displays an exceptional stability for ORR and excellent methanol tolerance, superior to that of 20 wt% Pt/C. Thus, this methodology might offer a way to develop cost-efficient non-noble metal catalysts with high ORR performance.

Author contributions

The work was accomplished through the contributions of all the authors. Preparation of Fe/Co/N–C/graphene and most of the electrochemical performance tests were contributed by Junchao Xiong, Yafei Zheng, Yupan Zhang. Yue Lu, Xundao Liu Yongming Zhang, Prof. Jun Lin and Dr Xiaohong Chen guided the entire process of the system and made revisions to the manuscript. All the authors agreed on the final version of the manuscript.

Conflicts of interest

There are no conflicts to declare.

Acknowledgements

This work was financially supported by the National Key R&D Program of China (2020YFB1505500).

References

1 L. Lei, Z. Tao, X. Wang, L. John and F. Chen, *J. Mater. Chem. A*, 2017, **5**, 22945–22951.
2 A. A. Gewirth and M. S. Thorum, *Inorg. Chem.*, 2010, **49**, 3557–3566.
3 M. Jang, M. Ciobotaru and V. G. Agelidis, *IEEE. T. Ind. Inform.*, 2013, **2**, 1158–1166.
4 Y. Wang, D. F. R. Diaz, K. S. Chen, Z. Wang and X. C. Adroher, *Mater*, 2020, **32**, 178–203.
5 Q. Liu, Q. Kang, Z. Wang, Q. Lu and F. Gao, *Dalton Trans.*, 2021, **50**, 6297–6305.
6 Y. Z. Chan, Y. Dai, R. Li, J. L. Zou, G. H. Tian and H. G. Fu, *Carbon*, 2015, **89**, 8–19.
7 L. Huang, S. Zaman, X. L. Tian, Z. T. Wang, W. S. Fang and B. Y. Xia, *Acc. Chem. Res.*, 2021, **54**, 311–322.
8 H. J. Meng, X. H. Chen, T. L. Gong, H. R. Liu, Y. M. Liu, H. Li and Y. M. Zhang, *Chem*, 2019, **11**, 6015–6021.
9 S. Sui, X. Y. Wang, X. T. Zhou, Y. H. Su, S. Riffatc and C. J. Liu, *J. Mater. Chem. A.*, 2017, **5**, 1808–1825.
10 A. Sokka, M. Mooste, M. Käärik, V. Gudkova, J. Kozlova, A. Kikas, V. Kisand, A. Treshchalov, A. Tamm, P. Paiste, J. Aruväli, J. Leis, A. Krumme, S. Holdcroft, S. Cavaliere, F. Jaouen and K. Tammeveski, *Int. J. Hydrogen Energy*, 2021, **46**, 31275–31287.
11 Y. Chen, L. Liang, S. Navia, A. Hinerman and X. Song, *ACS Catal.*, 2019, **9**, 6664–6684.
12 M. H. Shao, Q. W. Chang, J. P. Dodelet and R. Chenitz, *Chem. Rev.*, 2016, **116**, 3594–3657.
13 D. Y. Chung, J. M. Yoo and Y. E. Sung, *Adv. Mater.*, 2018, **30**, 170–182.
14 K. Wang, J. Liu, Z. Tang, L. Li and N. M. Bedford, *J. Mater. Chem. A*, 2021, **22**, 13044–13055.
15 W. Gu, L. Hu, L. Jing and E. Wang, *J. Mater. Chem. A.*, 2016, **4**, 14364–14370.
16 L. Ling, Q. Zhu and A. W. Xu, *J. Am. Chem. Soc.*, 2014, **136**, 11027–11033.
17 A. Sarapuu, E. Kibena-Poldsepp, M. Borghei and K. Tammeveski, *J. Mater. Chem. A*, 2018, **6**, 776–804.
18 J. Liang, Z. Yao, J. Chen, J. Liu, D. Hulicova-Jurcakova, M. Jaroniec and S. Z. Qiao, *Angew. Chem., Int. Ed.*, 2012, **51**, 3892–3896.
19 T. Tang, L. Ding, Z. Jiang, J. S. Hu and L. J. Wan, *Sci. China: Chem.*, 2020, **63**, 1517–1542.
20 S. Yuan, L. Cui, Z. Dou, X. Ge, X. He, W. Zhang and T. Asefa, *Small*, 2020, **16**, 2000742.
21 X. Chen, Z. Ning, Z. Zhou, X. Liu, J. Lei, S. Pei and Y. Zhang, *RSC Adv.*, 2018, **8**, 27246–27252.
22 D. Malko and A. Kucernak, *Electrochem. Commun.*, 2017, **83**, 67–71.
23 J. P. Xuan, N. B. Huang, J. J. Zhang, W. J. Dong and B. Wang, *J. Solid State Chem.*, 2020, **294**, 1572–1580.

24 D. Sebastian, V. Baglio, A. S. Arico, A. Serov and P. Atanassov, *Appl. Catal., B*, 2016, **182**, 297–305.
25 B. Li, Y. Chen, X. M. Ge, J. W. Chai, X. Zhang, T. S. A. Hor, G. J. Du, Z. L. Liu, H. Zhang and Y. Zong, *Nano*, 2016, **8**, 5067–5075.
26 S. S. A. Shah, L. S. Peng, T. Najam, C. Cheng, G. P. Wu, Y. Nie, W. Ding, X. Q. Qi, S. G. Chen and Z. D. Wei, *Electrochim. Acta*, 2017, **251**, 498–504.
27 H. Wang, C. C. Weng and Z. Y. Yuan, *J. Eng. Chem.*, 2020, **5**, 470–485.
28 M. Han, M. Shi, J. Wang, M. Zhang and Z. Guo, *Carbon*, 2019, **153**, 575–584.
29 C. Zhu, Q. Shi, B. Z. Xu, S. Fu, G. Wan, C. Yang, S. Yao, J. Song, H. Zhou, D. Du, S. P. Beckman, D. Su and Y. Lin, *Adv. Energy Mater.*, 2018, **8**, 1801956.
30 S. Zhao, J. Yang, M. Han, X. Wang and J. Bao, *Appl. Catal., B*, 2019, **260**, 118–207.
31 X. Wu, X. Yu, Z. Lin, J. Huang, L. Cao, B. Zhang, Y. Zhan, H. Meng, Y. Zhu and Y. Zhang, *Int. J. Hydrogen Energy*, 2016, **41**, 14111–14112.
32 Y. Wu, Y. Chen, H. Wang, C. Wang, A. Wang, Z. Shuai, X. Li, D. Sun and J. Jiang, *J. Mater. Chem. A*, 2018, **6**, 12018–12028.
33 H. T. Chung, J. H. Won and P. Zelenay, *Nat. Commun.*, 2013, **4**, 1922–1927.
34 Q. Cheng, S. Han, K. Mao, C. Chi, L. Yang, Z. Zou, G. Meng, H. Zheng and Y. Hui, *Nano Energy*, 2018, **52**, 485–493.
35 Y. Chen, C. Wang, Z. Wu, Y. Xiong, Q. Xu, S. Yu and H. Jiang, *Adv. Mater.*, 2015, **34**, 5010–5016.
36 S. Chao, Q. Xia, Y. Wang, W. Li and W. Chen, *Dalton Trans.*, 2020, **49**, 433–441.
37 H. F. Wang, L. Chen, H. Pang, S. Kaskel and Q. Xu, *Chem. Soc. Rev.*, 2020, **49**, 1039–1045.
38 W. Zhang, X. Yao, S. Zhou, X. Li and G. Lin, *Small*, 2018, **14**, 1870109.
39 X. X. Wang, D. A. Cullen, Y.-T. Pan, S. Hwang, M. Wang, Z. Feng, J. Wang, M. H. Engelhard, H. Zhang, Y. He, Y. Shao, D. Su, K. L. More, J. S. Spendelow and G. Wu, *Adv. Mater.*, 2018, **30**, 1706758.
40 J. Zhang, T. Zhang, K. Xiao, C. Sheng and F. Yi, *Cryst. Growth Des.*, 2016, **16**, 6494–6498.
41 W. Xia, C. Qu, Z. Liang, B. Zhao, S. Dai, B. Qiu, Y. Jiao, Q. Zhang, X. Huang and W. Guo, *Nano Lett.*, 2017, **17**, 2788–2795.
42 H. Su, S. Zhou, X. Zhang, H. Sun, H. Zhang, Y. Xiao, K. Yu, Z. Dong, X. Dai and X. Huang, *Dalton Trans.*, 2018, **47**, 16567–16577.
43 L. Zou, G. Zhong, Y. Nie, Z. Tan, W. Liao, X. Fu and Z. Pan, *Energy Technol.*, 2021, **9**, 2100035.
44 T. Palaniselvam, B. P. Biswal, R. Banerjee and S. Kurungot, *Chem. –Eur. J.*, 2013, **19**, 9335–9342.
45 Z. Liang, Q. Chong, W. Guo, R. Zou and Q. Xu, *Adv. Mater.*, 2018, **30**, 187–276.
46 Z. Zhu, C. Chen, M. Cai, Y. Cai, H. Ju, S. Hu and M. Zhang, *Mater. Res. Bull.*, 2019, **114**, 161–169.
47 R. Wang, P. Zhang, Y. Wang, Y. Wang, K. Zaghib and Z. Zhou, *Prog. Nat. Sci.: Mater. Int.*, 2020, **30**, 855–860.
48 L. Li, J. He, W. Ying, X. Lv, G. Xin, P. Dai, D. Liu and X. Zhao, *J. Mater. Chem. A*, 2019, **7**, 1964–1988.
49 Q. Wang, Z. Zhang, S. Shi, F. Wu, Z. Zhang, G. Li and Y. Suo, *J Electro Chem*, 2021, **894**, 115379.
50 Y. Jing, Y. Chen, L. Wang, Y. Liu, B. Yu and C. Yang, *Chem. Eng. J.*, 2020, **397**, 125539.
51 Y. Suo, Z. Zhang, Z. Zhang and G. Hu, *Ionics*, 2021, **27**, 1–15.
52 X. Chen, S. Zhang, L. Zhang, P. Zhu and G. Zhang, *Polymers*, 2021, **13**, 482–496.
53 Y. Liu, H. Shen, H. Jiang, W. Li, J. Li, Y. Li and Y. Guo, *Int. J. Hydrogen Energy*, 2017, **42**, 12978–12988.
54 H. Zhong, J. Wang, Y. Zhang, W. Xu, W. Xing, D. Xu and Y. Zhang, *Angew. Chem., Int. Ed.*, 2014, **51**, 14235–14239.
55 Y. Dong, S. Liao, H. Song, J. Zeng and Y. Deng, *J. Mater. Chem. A*, 2017, **5**, 5829–5837.
56 G. Zhang, Y. Xu, X. Xiang, G. Zheng, X. Zeng, Z. Li, T. Ren and Y. Zhang, *Tribol. Int.*, 2018, **126**, 39–48.
57 F. C. Tai, C. Wei, S. H. Chang and W. S. Chen, *J. Raman Spectrosc.*, 2010, **41**, 933–937.
58 F. Liu, F. Niu, T. Chen, J. Han, Z. Liu, W. Yang, Y. Xu and J. Liu, *Carbon*, 2018, **134**, 316–325.
59 X. Leng, X. Ding, J. Hu, S. Wei, Z. Jiang, J. Lian, G. Wang, Q. Jiang and J. Liu, *Electro. Acta*, 2016, **190**, 276–284.
60 X. Chen, Z. Xue, K. Niu, X. Liu, W. lv, B. Zhang, Z. Li, H. Zeng, Y. Ren, Y. Wu and Y. Zhang, *RSC Adv.*, 2021, **11**, 4053–4061.
61 H. Huang, Y. Li, N. Wang, S. Chen, C. Wang and T. Ma, *Inorg. Chem. Commun.*, 2019, **101**, 23–26.
62 Q. Shi, Q. Liu, Y. Ma, Z. Fang, Z. Liang, G. Shao, B. Tang, W. Yang, L. Qin and X. Fang, *Adv. Energy Mater.*, 2020, **10**, 1903854.